



In situ assembly of BiOI@Bi₁₂O₁₇Cl₂ *p-n* junction: charge induced unique front-lateral surfaces coupling heterostructure with high exposure of BiOI {001} active facets for robust and nonselective photocatalysis

Hongwei Huang^{a,*}, Ke Xiao^a, Ying He^a, Tierui Zhang^b, Fan Dong^c, Xin Du^d, Yihe Zhang^{a,*}

^a Beijing Key Laboratory of Materials Utilization of Nonmetallic Minerals and Solid Wastes, National Laboratory of Mineral Materials, School of Materials Science and Technology, China University of Geosciences, Beijing, 100083, China

^b Key Laboratory of Photochemical Conversion and Optoelectronic Materials, Technical Institute of Physics and Chemistry, Chinese Academy of Sciences, Beijing, 100190, China

^c Chongqing Key Laboratory of Catalysis and Functional Organic Molecules, College of Environmental and Bio-logical Engineering, Chongqing Technology and Business University, Chongqing, 400067, China

^d Research Center for Bioengineering and Sensing Technology, Department of Chemistry & Biological Engineering, University of Science & Technology Beijing, Beijing, 100083, China

ARTICLE INFO

Article history:

Received 20 April 2016

Received in revised form 2 June 2016

Accepted 5 June 2016

Available online 6 June 2016

Keywords:

Heterostructure

p-n junction

Active facets

BiOI

Bi₁₂O₁₇Cl₂

ABSTRACT

Synthesis of reactive exposing facets and *p-n* junction are of great importance for semiconductor photocatalysis. Herein, we develop a *p-n* junction BiOI@Bi₁₂O₁₇Cl₂ heterostructure via facilely *in situ* depositing BiOI nanosheets on the surface of Bi₁₂O₁₇Cl₂ plates. Owing to the charge inducement, the BiOI nanosheets are all vertically assembled onto the Bi₁₂O₁₇Cl₂ large plates to form a unique front-lateral surfaces coupling heterostructure, which enables high exposure of {001} reactive exposing facets of BiOI. The photocatalytic properties are systematically evaluated by degrading multiform industrial contaminants and antibiotic, like 2,4-dichlorophenol (2,4-DCP), rhodamine B (RhB), phenol, bisphenol A (BPA), and tetracycline hydrochloride. It reveals that the BiOI@Bi₁₂O₁₇Cl₂ heterostructure not only shows dramatically strengthened photocatalytic activity, but also unfold powerful and nonselective photooxidation ability under visible-light illumination. The photoelectrochemical characterizations demonstrated that the drastically promoted separation and transfer of charge carriers that derived from the benefits of BiOI {001} active facets and BiOI@Bi₁₂O₁₇Cl₂ *p-n* junction are in charge of the high photo-activity. Detailed radicals detection and quantification experiments further corroborate our conclusions. The study may give us some new hints on designing novel heterostructured photoelectronic materials with integrating *p-n* junction and active exposing facets.

© 2016 Elsevier B.V. All rights reserved.

1. Introduction

Semiconductor photocatalysis as a green technology has garnered particular attention for splitting water into hydrogen and oxygen, eliminating various kinds of contaminants and/or inactivating viruses with light illumination [1–3]. To efficaciously make use of the largest proportion of the solar spectrum (visible light, $\lambda > 400$ nm), numerous visible-light-responsive (VLR) photocatalysts have been developed [4–6]. Nevertheless, a single VLR photocatalyst always suffers from some drawbacks, such as fast

recombination of photo-excited electrons and holes. Developing new VLR photocatalyst systems for meeting the pressing need in environmental and energy areas is thus of great significance.

Construction of heterostructured semiconductor phase-junctions has recently been very active because of its perfect effectiveness in promoting the separation of photogenerated charge carriers and improving the photocatalysis property [7–11]. In particular, heterostructured photocatalysts containing *p-n* junctions with direct contact between *p*-type and *n*-type semiconductors have received broad attention because the large potential gradient and built-in electron field established at the junction level could induce efficient charge separation, as illustrated by the *p-n* junctions of Co₃O₄/BiVO₄ [12], NiO/TiO₂ [13], etc. Another effective approach to enhancing photocatalysis performance is

* Corresponding authors.

E-mail addresses: hwh@cugb.edu.cn (H. Huang), zyh@cugb.edu.cn (Y. Zhang).

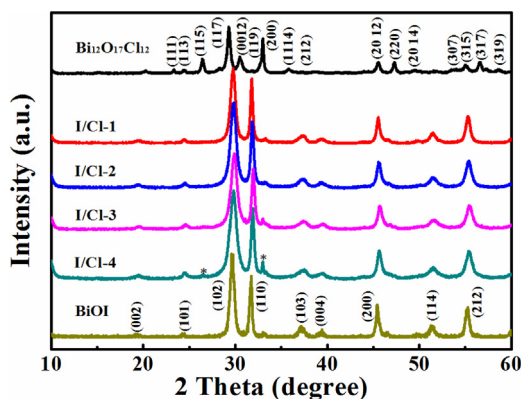


Fig. 1. XRD patterns of $\text{Bi}_{12}\text{O}_{17}\text{Cl}_2$, BiOI and $\text{BiOI}@\text{Bi}_{12}\text{O}_{17}\text{Cl}_2$ composites.

crystal facet engineering. For instance, it has been demonstrated that anatase TiO_2 with exposed {001} reactive facets possesses the high photooxidative ability [14]. Gordon et al. reported that the TiO_2 nanocrystals obtained by a seeded growth method with the {101} exposing facets shows more reactive photocatalytic water splitting performance [15]. Recently, Yu et al. have optimized the photocatalytic property of TiO_2 for the CO_2 reduction into CH_4 through engineering the ratio of the exposed {101} facet to {001} facet of TiO_2 , and meanwhile demonstrated that excessive exposure of {101} or {001} facets all lead to the fast recombination of electrons and holes [16].

Recently, bismuth halide photocatalytic materials show great potentials for their strong oxidation ability, high stability, etc. The large family of bismuth halide photocatalysts include not only the Sillescu-structured BiOX ($X = \text{F}, \text{Cl}, \text{Br}, \text{I}$) series [17–21], but also the non-stoichiometric $\text{Bi}_3\text{O}_4\text{Cl}$ [22], $\text{Bi}_{12}\text{O}_{17}\text{Cl}_2$ [23], $\text{Bi}_3\text{O}_4\text{Br}$ [24], $\text{Bi}_5\text{O}_7\text{I}$ [25], $\text{Bi}_4\text{O}_5\text{I}_2$ [26], etc. Among them, the Sillescu-family member BiOI displays promising prospect for its narrowest bandgap (1.7–1.9 eV) in the bismuth halide materials [27,28]. Though substantial work demonstrated that the photo-activity of BiOI can be enhanced by fabricating heterojunctions, like TiO_2/BiOI [29], ZnO/BiOI [30], $\text{BiPO}_4/\text{BiOI}$ [31], BiOCl/BiOI [32] and BiOBr/BiOI [33] and the highly efficient *p-n* junction $\text{BiVO}_4/\text{BiOI}$ [34,35]. On the other hand, the controlled synthesis of BiOI with exposed {001} active facets enables it much improved photocatalytic activity [36,37]. Nevertheless, developing absorbing BiOI heterostructure with exposed active facets has not been achieved. Lately, we have developed a facile ethylene-glycol assisted room-temperature precipitation route to preparing the *p*-type BiOI microsphere, which are self-assembled by numerous BiOI nanosheets with {001} reactive exposing facets [38–40]. However, most BiOI nanosheets are wrapped inside the microsphere, which are inactivated in the photocatalytic process as the photochemical reaction is surface reaction. Therefore, manufacturing an efficient *p-n* junction by compositing BiOI with a suitable *p*-type semiconductor to obtain an elaborate heterostructure with evenly distributed {001}-facet-exposed BiOI nanosheets is challenging and highly anticipated.

In this work, we first prepare $\text{Bi}_{12}\text{O}_{17}\text{Cl}_2$ plates with even surface, and then simply *in situ* deposit BiOI nanosheets on the surface of $\text{Bi}_{12}\text{O}_{17}\text{Cl}_2$ to fabricate a $\text{BiOI}@\text{Bi}_{12}\text{O}_{17}\text{Cl}_2$ *p-n* junction. Interestingly, the BiOI nanosheets are all vertically inserted into the $\text{Bi}_{12}\text{O}_{17}\text{Cl}_2$ large plates owing to the charge induction effect between the BiOI lateral surface and $\text{Bi}_{12}\text{O}_{17}\text{Cl}_2$ front surface. This unique front-lateral surfaces coupling heterostructure enables the high exposure of {001} reactive exposing facets of BiOI. The photocatalysis performance of the heterostructured $\text{BiOI}@\text{Bi}_{12}\text{O}_{17}\text{Cl}_2$ *p-n* junction is systematically investigated by degradation of various contaminants and antibiotic, including Rho-

damine B (RhB), 2,4-dichlorophenol (2,4-DCP), phenol, bisphenol A (BPA), and tetracycline hydrochloride, and the results indicate that the $\text{BiOI}@\text{Bi}_{12}\text{O}_{17}\text{Cl}_2$ *p-n* junction shows greatly enhanced photo-activity. To inspect origin for the high activity, a series of photoelectrochemical measurements are conducted. Additionally, active species detection and $\cdot\text{O}_2^-$ quantification experiments are also performed to figure out the photoreaction mechanism. Based on the results from the above experiments, the remarkably enhanced photochemical and photoelectrochemical properties are analyzed. Our work may shed new light on development of novel heterostructured *p-n* junction photocatalysts with exposing active facets.

2. Experimental

2.1. Synthesis of $\text{BiOI}@\text{Bi}_{12}\text{O}_{17}\text{Cl}_2$ heterostructure

The raw materials are all in analytical grade and used without further purification. $\text{Bi}_{12}\text{O}_{17}\text{Cl}_2$ was first prepared by a hydrothermal process. $\text{Bi}(\text{NO}_3)_3 \cdot 5\text{H}_2\text{O}$ (1 mmol) and KCl (1 mmol) was dissolved into 30 ml deionized water under vigorously stirring, and then the pH value of above suspension was adjusted to 13 by slow dripping of 1 mol/L NaOH solution. After being stirred for 30 min, the obtained solution was transferred into a 50 mL Teflon autoclave and maintained at 160°C for 24 h. After cooling, the products were collected by filtration and washed repeatedly with deionized water and ethanol and then dried at 80°C for 10 h.

The $\text{BiOI}@\text{Bi}_{12}\text{O}_{17}\text{Cl}_2$ heterostructures were synthesized by a facile ethylene glycol (EG)-assisted *in situ* precipitation method at room temperature. $\text{Bi}_{12}\text{O}_{17}\text{Cl}_2$ was first dispersed in 25 ml EG containing certain amount of $\text{Bi}(\text{NO}_3)_3 \cdot 5\text{H}_2\text{O}$. Then, 25 ml of stoichiometric KI water solution was dropwise added into the above suspension, and was kept stirring for 3 h. After that, the products were filtrated and washed repeatedly with deionized water and ethanol, and dried at 80°C for 5 h. The $\text{BiOI}@\text{Bi}_{12}\text{O}_{17}\text{Cl}_2$ composites with $\text{Bi}_{12}\text{O}_{17}\text{Cl}_2$:BiOI molar ratios of 40%, 30%, 20% and 10% are named as I/Cl-1, I/Cl-2, I/Cl-3 and I/Cl-4, respectively. Pure BiOI sample was prepared by the same procedure with no addition of $\text{Bi}_{12}\text{O}_{17}\text{Cl}_2$.

2.2. Characterization

X-ray diffraction (XRD) was performed to examine the crystal structure of samples by a Cu K α radiation Bruker D8 Advance diffractometer. The surface states and composition of elements are examined by a Perkin-Elmer PHI 5000C X-ray photoelectron spectroscopy (XPS). Scanning electron microscopy (SEM, S-4800) and transmission electron microscopy (TEM, high-resolution TEM, JEM-2100F) are employed to observe the morphology and microstructure. UV–vis diffuse reflectance spectra (DRS) were recorded on a UV–vis spectrophotometer (Varian Cary 5000). The zeta potentials of samples are determined on a 90Plus Zeta potential instrument.

2.3. Photocatalytic assessments

The photocatalysis properties of samples are evaluated via degradation of multiple industrial contaminants and antibiotic, such as rhodamine B (RhB, 0.02 mM), 2,4-dichlorophenol (2,4-DCP, 10 mg/L), bisphenol A (BPA, 10 mg/L), phenol (10 mg/L) and tetracycline hydrochloride (10 mg/L) under visible light irradiation (500 W Xe lamp, $\lambda > 420$ nm).

The photodegradation processes are shown as follows: 50 mg catalyst was ultrasonic dispersed into 50 ml solutions containing the RhB, 2,4-DCP, BPA, phenol and tetracycline hydrochloride. Before exposure to light, the suspensions were stirred for 1 h in

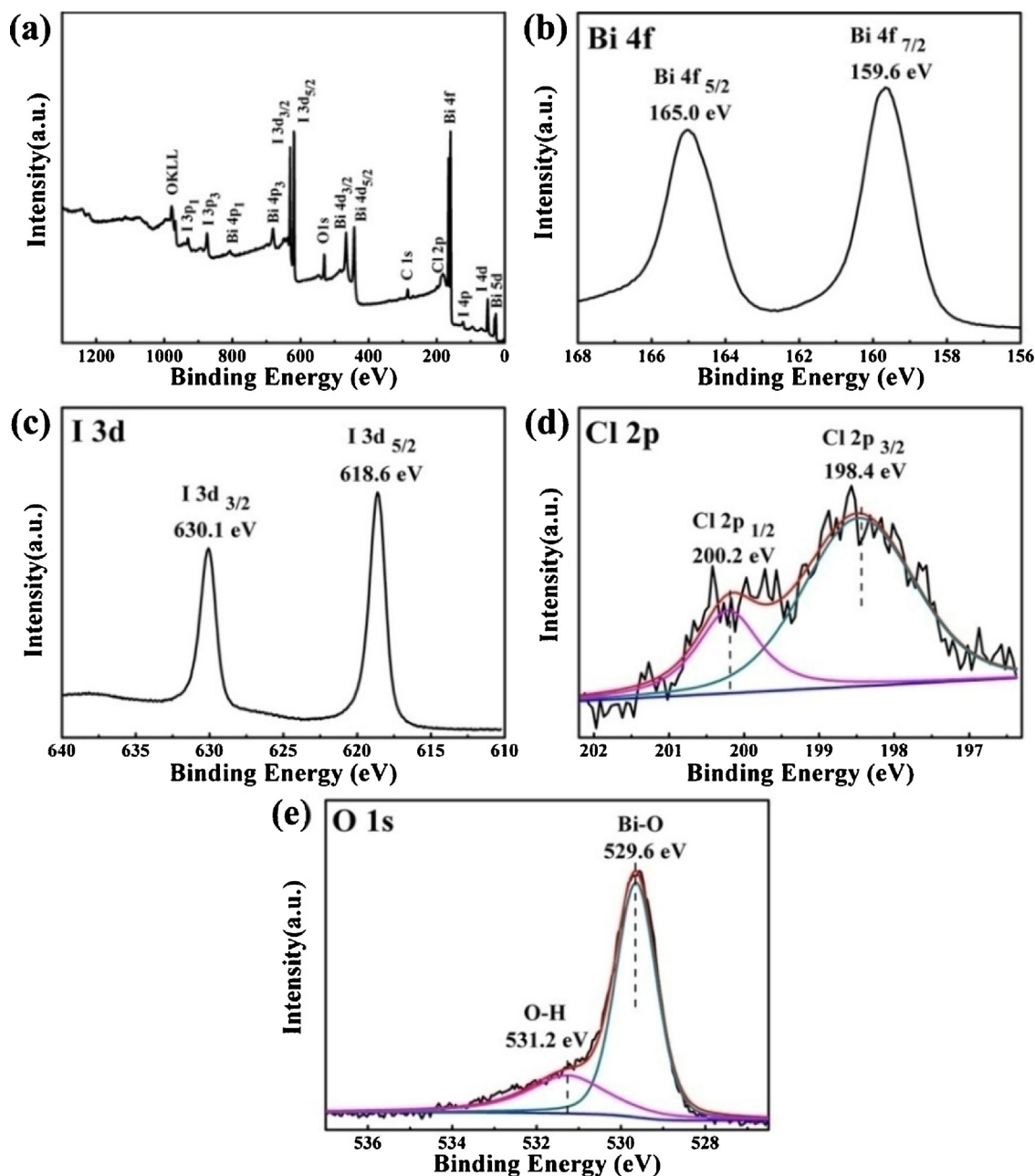


Fig. 2. XPS spectra of the BiOI@Bi₁₂O₁₇Cl₂ composite (I/Cl-2): (a) survey, (b) Bi 4f, (c) I 3d, (d) Cl 2p and (e) O 1s.

darkness to achieve an adsorption-desorption balance between catalyst and pollutant. At certain intervals, about 2–3 ml suspension was extracted and centrifuged to get rid of the solid. Then, the supernatant liquid was analyzed by recording the change of the characteristic absorbance bands of pollutants on a UV–vis spectrophotometry (Cary 5000). The total organic carbon (TOC) removal of RhB was determined on a total organic carbon analyzer (TOC, Shimadzu 500).

2.4. Photoelectrochemical measurements

Photocurrent density, Mott-Schottky curves and electrochemical impedance spectra (EIS) were all obtained on an electrochemical system (CHI-660E, China) in a three-electrode quartz cells. The saturated calomel electrode (SCE) was used as the reference electrode, and the counter electrode was platinum wires. The working electrode was the sample films (BiOI, Bi₁₂O₁₇Cl₂ and I/Cl-2) coated on

ITO glasses. The light source is a 300 W Xe lamp with 420 nm filters to exclude the UV light, and 0.1 M Na₂SO₄ was used as the electrolyte.

2.5. Active species detection and •O₂[−] quantification experiments

Active species generated in the photocatalytic reaction process are detected by trapping agent. Holes (h⁺), hydroxyl radical (•OH) and superoxide radical (•O₂[−]) can be consumed by addition of ethylene diamine tetraacetic acid disodium salt (EDTA-2Na, 1 mM), iso-propanol (IPA, 1 mM) and benzoquinone (BQ, 1 mM), respectively [41,42].

•O₂[−] quantification experiment was conducted by reacting with NBT (0.025 mM) which displays a maximum absorbance at 260 nm to determine the amount of •O₂[−] produced from BiOI, Bi₁₂O₁₇Cl₂ and I/Cl-2 [42]. This experiment is similar to the above photodegra-

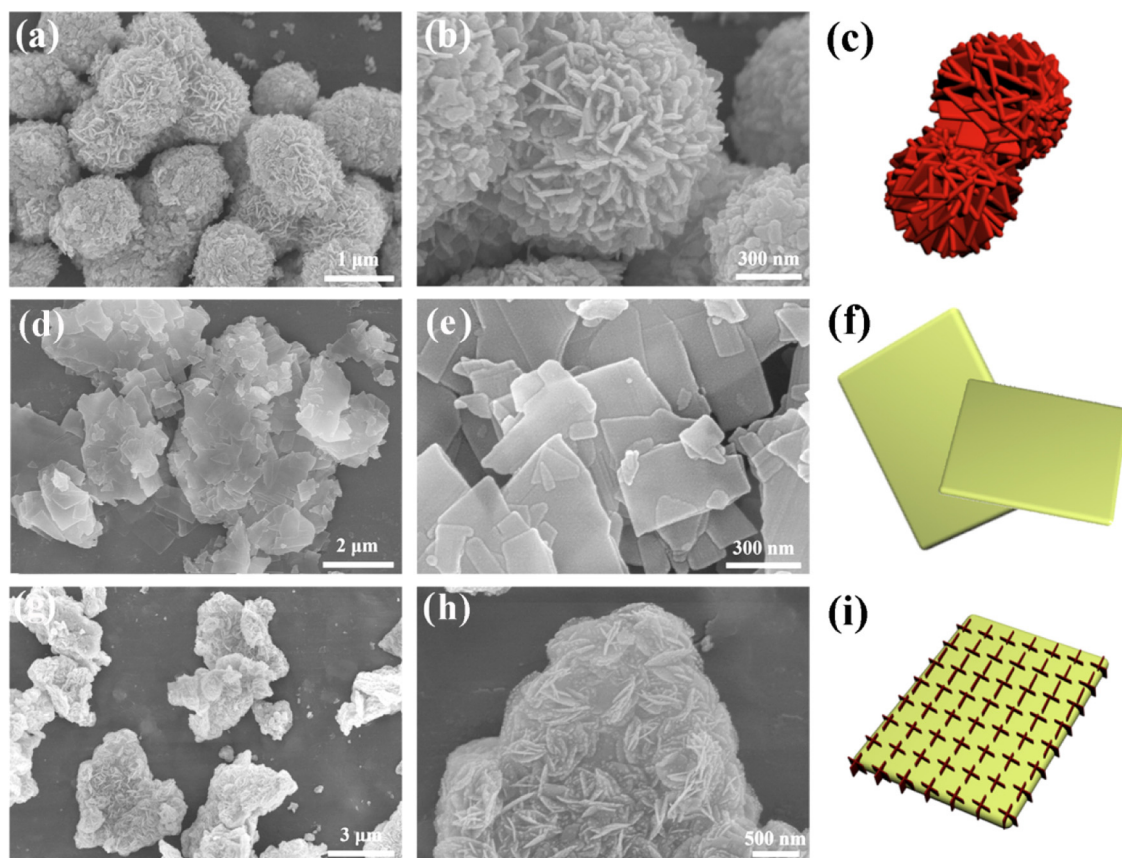


Fig. 3. SEM images of (a, b) BiOI, (d, e) Bi₁₂O₁₇Cl₂ and (g, h) BiOI@Bi₁₂O₁₇Cl₂ architecture (I/Cl-2); schematic diagrams of (c) BiOI, (f) Bi₁₂O₁₇Cl₂ and (i) BiOI@Bi₁₂O₁₇Cl₂ architecture.

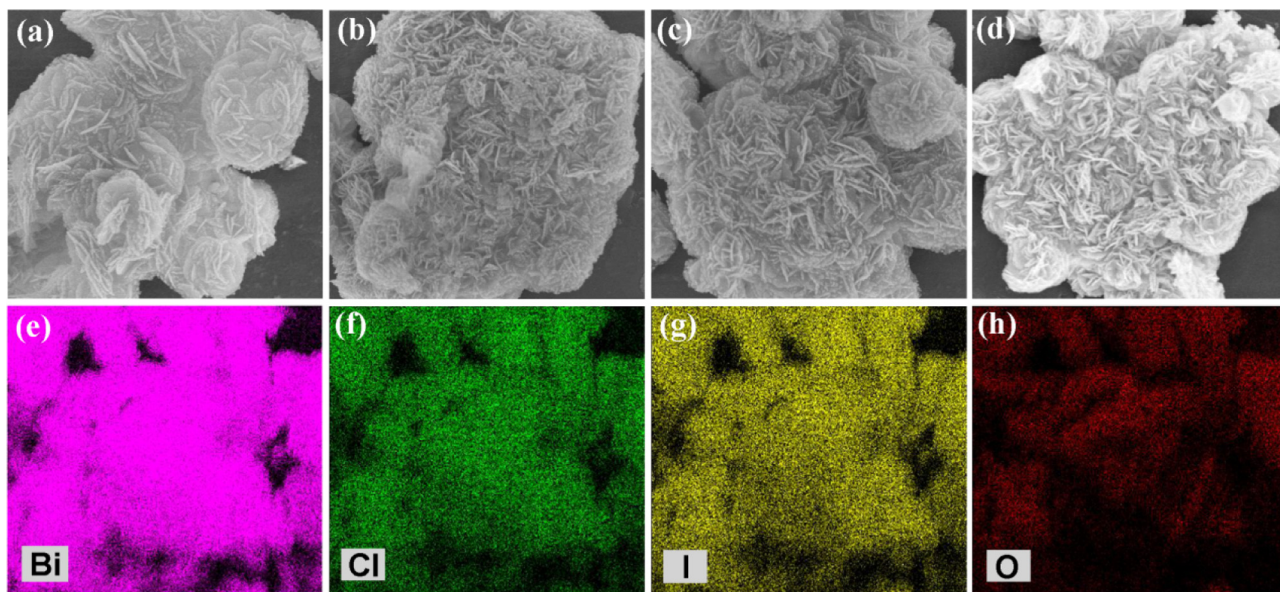


Fig. 4. SEM images of BiOI@Bi₁₂O₁₇Cl₂ composites: (a) I/Cl-1, (b) I/Cl-2, (c) I/Cl-3 and (d) I/Cl-4; (e–h) EDX-mapping images of I/Cl-2.

dation one except that RhB was replaced by NBT. The concentration change of NBT is examined on a 5000 UV–vis spectrophotometer.

3. Results and discussion

3.1. Crystal structure and composition

The crystal structures of Bi₁₂O₁₇Cl₂, BiOI and BiOI@Bi₁₂O₁₇Cl₂ composites are determined by XRD. As shown in Fig. 1, the diffrac-

tion peaks of Bi₁₂O₁₇Cl₂ and BiOI can be ascribed to the tetragonal Bi₁₂O₁₇Cl₂ (JCPDS #37-0702) and tetragonal BiOI (JCPDS #10-0445), respectively. As for the BiOI@Bi₁₂O₁₇Cl₂ composites, most of peaks belong to BiOI, which is due to the major content of BiOI. With the increase of Bi₁₂O₁₇Cl₂ content, the intensities of the (115) and (200) peaks of Bi₁₂O₁₇Cl₂ at 26.4° and 33.0° gradually strengthen in the patterns of BiOI@Bi₁₂O₁₇Cl₂ composites. This result demonstrates the successful synthesis of BiOI@Bi₁₂O₁₇Cl₂ composites.

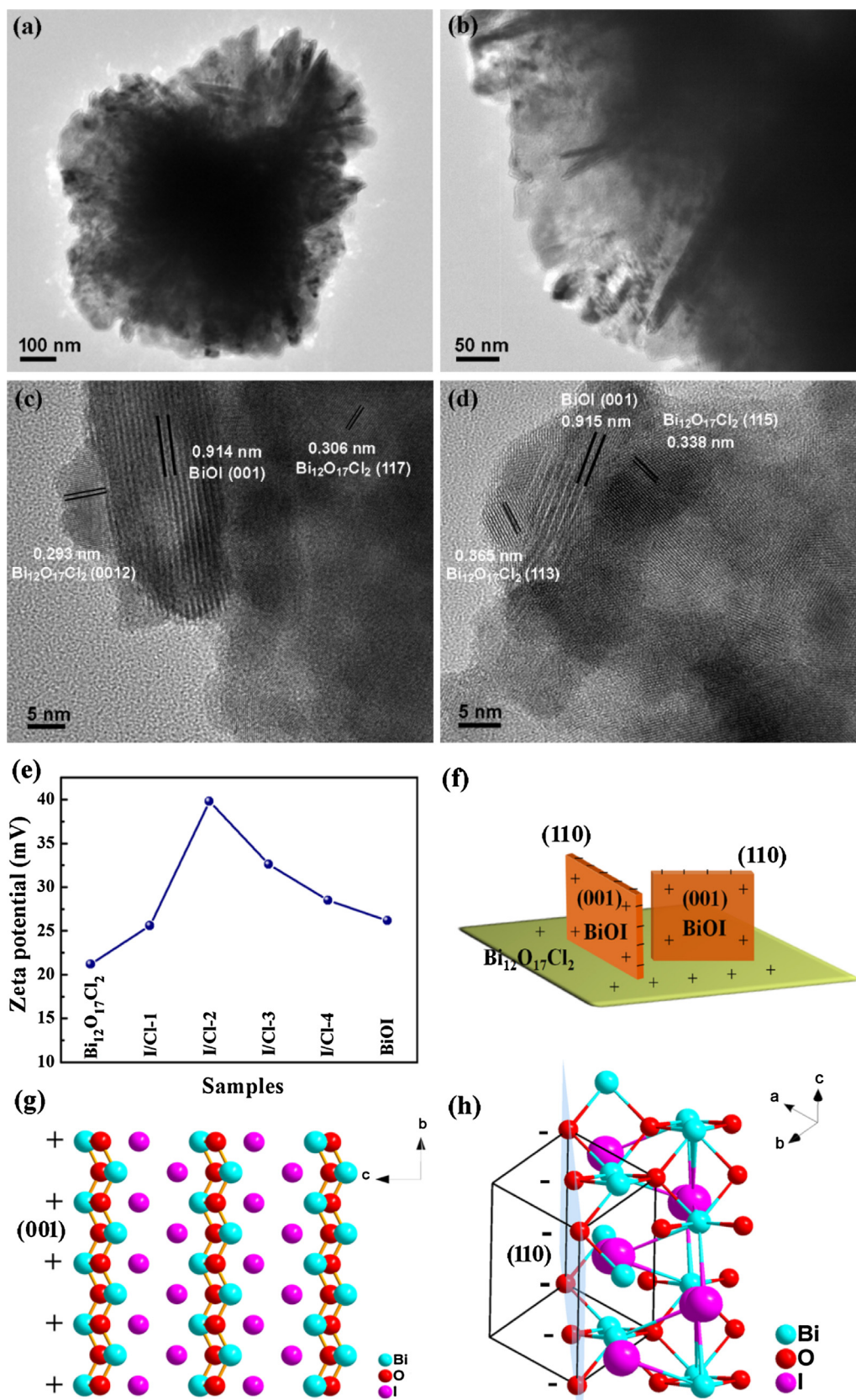


Fig. 5. (a, b) TEM images of I/Cl-2, (c, d) HR-TEM images of I/Cl-2, (e) Zeta potentials of samples. (f) Schematic diagram of BiOI@Bi₁₂O₁₇Cl₂ architecture. Crystal structure of BiOI with exposed (g) {001} facet and (h) {110} facet.

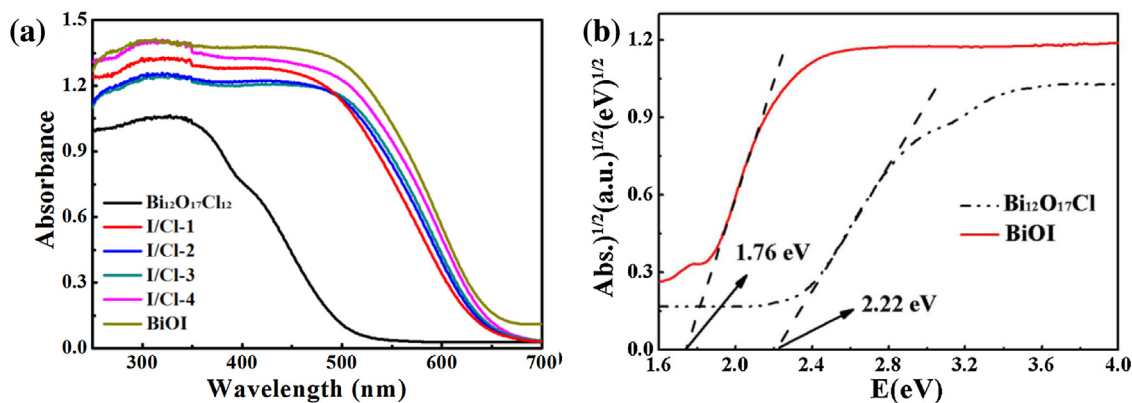


Fig. 6. (a) UV-vis diffuse reflectance spectra of $\text{Bi}_{12}\text{O}_{17}\text{Cl}_2$, BiOI and BiOI@ $\text{Bi}_{12}\text{O}_{17}\text{Cl}_2$ composites. (b) Band gaps of $\text{Bi}_{12}\text{O}_{17}\text{Cl}_2$ and BiOI.

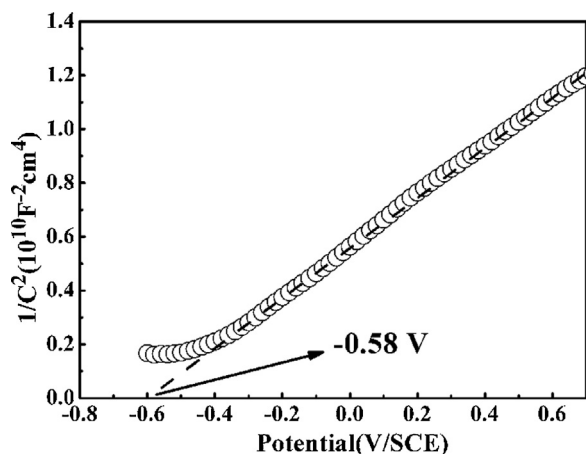


Fig. 7. Mott-Schottky curve of $\text{Bi}_{12}\text{O}_{17}\text{Cl}_2$.

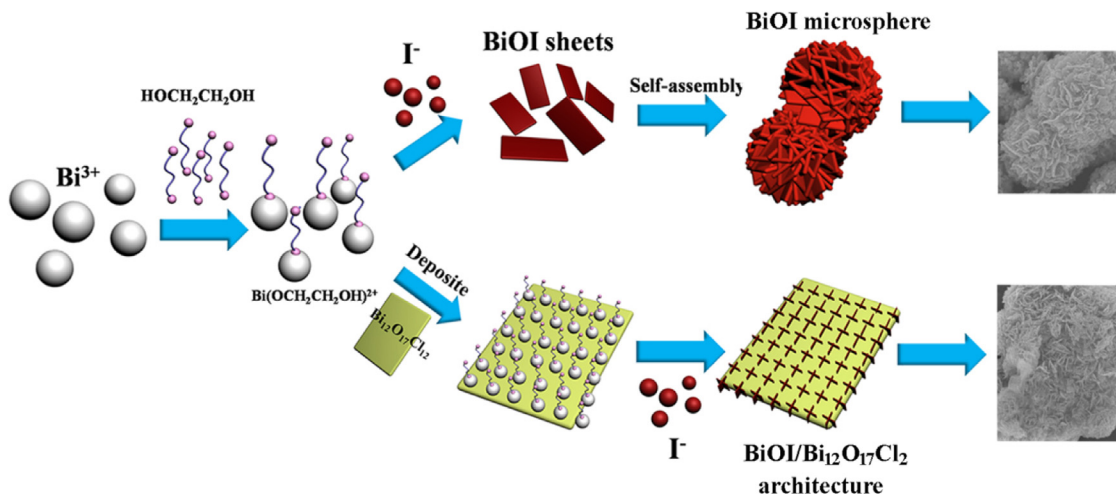
Fig. 2 shows the XPS pattern of the BiOI@ $\text{Bi}_{12}\text{O}_{17}\text{Cl}_2$ composite (I/Cl-2). As seen from Fig. 2a, the constituent elements Bi, O, Cl and I all can be detected. The two strong peaks at 165.0 and 159.6 eV are ascribed to the Bi $4f_{5/2}$ and Bi $4f_{7/2}$, respectively (Fig. 2b). The I 3d spectrum (Fig. 2c) shows two distinct peaks at 630.1 and 618.6 eV, which correspond to the I $3d_{3/2}$ and I $3d_{5/2}$ of BiOI, respectively [35]. Fig. 2d shows the Cl 2p peak of $\text{Bi}_{12}\text{O}_{17}\text{Cl}_2$. It can be deconvoluted into two peaks at 200.2 eV and 198.4 eV, which are attributed to the Cl $2p_{1/2}$ and Cl $2p_{3/2}$, respectively [36]. As shown in Fig. 2e, the

O 1s peak is deconvoluted into two peaks at 531.2 and 529.6 eV, and they are separately assigned to the O–H bond absorbed on the surface of sample and lattice Bi–O bond [33]. The XPS observation confirms the co-existence of $\text{Bi}_{12}\text{O}_{17}\text{Cl}_2$ and BiOI in the composites.

In order to determine the real loading amounts of BiOI on $\text{Bi}_{12}\text{O}_{17}\text{Cl}_2$, element analysis was performed over I/Cl-2 as a representative of BiOI@ $\text{Bi}_{12}\text{O}_{17}\text{Cl}_2$ heterostructures. The result demonstrated that the molar ratio of Cl:I in I/Cl-2 is 1:1.72, which is consistent with the theoretical value (molar ratio of $\text{Bi}_{12}\text{O}_{17}\text{Cl}_2$ to BiOI is 30%).

3.2. Investigations on the morphology and microstructure of the charge induced assembly heterostructures

The morphology and microstructure of $\text{Bi}_{12}\text{O}_{17}\text{Cl}_2$, BiOI and BiOI@ $\text{Bi}_{12}\text{O}_{17}\text{Cl}_2$ composites are observed by SEM. As seen from Fig. 3a and b, BiOI presents uniform microsphere structure and the diameter is about 1 μm . The BiOI microspheres are composed of plenty of nanosheets with size of 100–200 nm. Fig. 3d and e shows the SEM images of $\text{Bi}_{12}\text{O}_{17}\text{Cl}_2$ products, which consist of large smooth plates with size ranging from dozens of nanometers to several micrometers. The large and flat $\text{Bi}_{12}\text{O}_{17}\text{Cl}_2$ plates may provide a good platform for BiOI nanosheets to grow on. As shown in Fig. 3g and h, different from the BiOI microsphere and $\text{Bi}_{12}\text{O}_{17}\text{Cl}_2$ smooth plate, the BiOI@ $\text{Bi}_{12}\text{O}_{17}\text{Cl}_2$ composite (I/Cl-2) displays an interesting architecture, in which almost all the BiOI nanosheets are vertically inserted into the $\text{Bi}_{12}\text{O}_{17}\text{Cl}_2$ plate. This novel assembly not only enables intimate interfacial interaction, but also may offer



Scheme 1. Formation diagram of the BiOI microsphere and BiOI@ $\text{Bi}_{12}\text{O}_{17}\text{Cl}_2$ architecture.

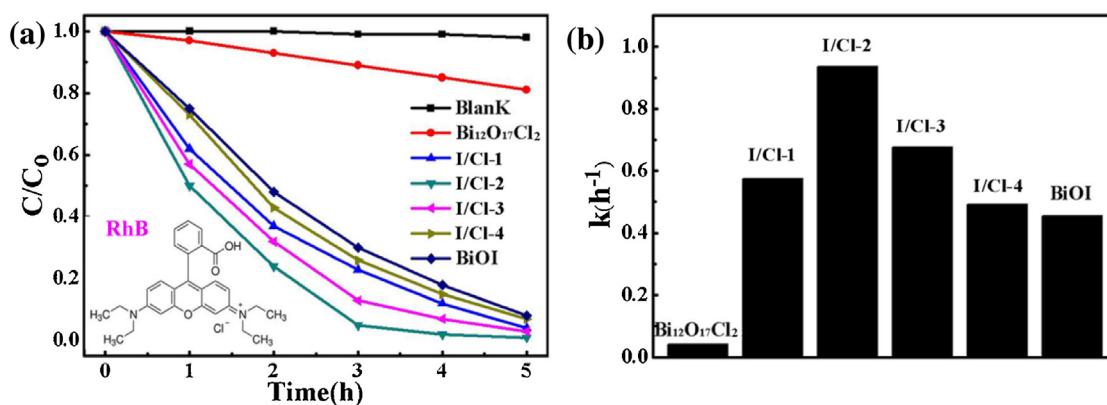


Fig. 8. (a) Photocatalytic degradation curves of RhB over BiOI, $\text{Bi}_{12}\text{O}_{17}\text{Cl}_2$ and $\text{BiOI@Bi}_{12}\text{O}_{17}\text{Cl}_2$ composites under visible light irradiation ($\lambda > 420 \text{ nm}$); (b) apparent rate constants.

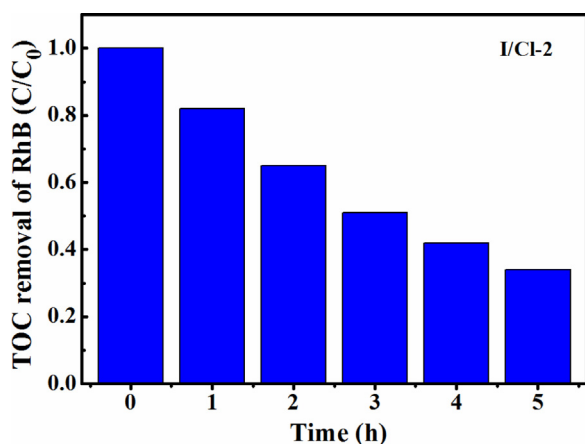


Fig. 9. TOC removal of RhB over I/Cl-2 under visible light illumination ($\lambda > 420 \text{ nm}$).

many other advantages. Fig. 3c, f and i illustrates the scheme of BiOI microspheres, $\text{Bi}_{12}\text{O}_{17}\text{Cl}_2$ plates and $\text{BiOI@Bi}_{12}\text{O}_{17}\text{Cl}_2$ heterostructure, which can obviously reflect their morphology features and difference.

Fig. 4a–d shows the SEM images of $\text{BiOI@Bi}_{12}\text{O}_{17}\text{Cl}_2$ composites with different BiOI contents (I/Cl-1, I/Cl-2, I/Cl-3 and I/Cl-4). When the relatively content of BiOI is low, the BiOI nanosheets are loosely inserted into the surface of $\text{Bi}_{12}\text{O}_{17}\text{Cl}_2$ (Fig. 4a). With increasing the BiOI amount, more and more nanosheets appear on $\text{Bi}_{12}\text{O}_{17}\text{Cl}_2$ and some of BiOI nanosheets are aggregated at its high content (I/Cl-4). To further illustrate the distribution of BiOI on $\text{Bi}_{12}\text{O}_{17}\text{Cl}_2$, EDX-mapping was conducted on I/Cl-2. As shown in Fig. 4e–h, the element of Bi, O, Cl and I all can be clearly observed, and their distributions are highly homogenous. It demonstrates that the BiOI nanosheets are uniformly embedded on the $\text{Bi}_{12}\text{O}_{17}\text{Cl}_2$ plates.

Based on the above SEM results, the formation process of BiOI microspheres and $\text{BiOI@Bi}_{12}\text{O}_{17}\text{Cl}_2$ architecture are proposed as illustrated in Scheme 1. Ethylene glycol can dissolve Bi^{3+} to be alkoxides ($\text{Bi}(\text{OCH}_2\text{CH}_2\text{OH})^{2+}$) and to form a clear and homogeneous solution [47]. As it react with I^- in the ethylene glycol/water solution, the BiOI nanosheets would immediately generate and further self-assemble to be microspheres to keep low surface energy. When the $\text{Bi}_{12}\text{O}_{17}\text{Cl}_2$ plates were introduced, ($\text{Bi}(\text{OCH}_2\text{CH}_2\text{OH})^{2+}$) encircles $\text{Bi}_{12}\text{O}_{17}\text{Cl}_2$. After adding KI solution, ($\text{Bi}(\text{OCH}_2\text{CH}_2\text{OH})^{2+}$) reacts with I^- and produce BiOI nanosheets. To minimize the surface energy, these nanosheets would *in situ* grow on the surface of the $\text{Bi}_{12}\text{O}_{17}\text{Cl}_2$ plates. Then, the $\text{BiOI@Bi}_{12}\text{O}_{17}\text{Cl}_2$ architecture was formed. To further elucidate the mechanism for formation of the interesting $\text{BiOI@Bi}_{12}\text{O}_{17}\text{Cl}_2$ heterostructure and obtain more

information, TEM and HRTEM are performed. Fig. 5a and b shows the TEM images of the $\text{BiOI@Bi}_{12}\text{O}_{17}\text{Cl}_2$ heterostructure (I/Cl-2), which confirmed that the BiOI nanosheets are vertically embedded on the large plate of $\text{Bi}_{12}\text{O}_{17}\text{Cl}_2$. For further confirmation, the HRTEM images are shown in Fig. 5c and d. As it can be seen, the slender lattice fringes with interplanar spacings of 0.293 nm, 0.306 nm, 0.338 nm and 0.365 nm correspond well to the (0012), (117), (115) and (113) planes of $\text{Bi}_{12}\text{O}_{17}\text{Cl}_2$, respectively. Among these lattice fringes of $\text{Bi}_{12}\text{O}_{17}\text{Cl}_2$, one can see a set of clear and coarse lattice fringe with a spacing of 0.914 nm or 0.915 nm, which can be indexed into the (001) facet of BiOI. Thus, the main exposed facet of BiOI is {001} facet, and BiOI assembled on the front surface of $\text{Bi}_{12}\text{O}_{17}\text{Cl}_2$ via the {110} facet of BiOI (lateral surface). It is worthy to note that this front-lateral surfaces coupling is obviously different from the most reported layered bismuth-based composites in which the nanosheets/plates are combined in a 2D–2D way [36,37].

In order to explore the reason for forming this unique assembly, we measured the Zeta potentials of $\text{Bi}_{12}\text{O}_{17}\text{Cl}_2$, I/Cl-1, I/Cl-2, I/Cl-3 and I/Cl-4 and BiOI, which are +21.2, +25.6, +39.8, +32.6, +28.5 and +26.2 mV, respectively (Fig. 5e). All the samples are positively charged, so that BiOI cannot assemble on $\text{Bi}_{12}\text{O}_{17}\text{Cl}_2$ in a front-front surface coupling way. As depicted in Fig. 5g, the outermost exposed atoms of {001} facet of BiOI is Bi^{3+} , and thus the {001} facet is positively charged. Comparatively, the {110} facet of BiOI is negatively charged as its outermost atoms are O atoms. Though the crystal structure of $\text{Bi}_{12}\text{O}_{17}\text{Cl}_2$ cannot be obtained, we conjecture that the (0012), (117), (115) and (113) planes of $\text{Bi}_{12}\text{O}_{17}\text{Cl}_2$ is mainly characterized by Bi atoms. Therefore, the $\text{BiOI@Bi}_{12}\text{O}_{17}\text{Cl}_2$ architecture is constructed through the coupling between the positively-charged front surface of $\text{Bi}_{12}\text{O}_{17}\text{Cl}_2$ and negatively-charged lateral surface of BiOI. Additionally, the as-measured Zeta potentials show a trend of first increase and then decrease. It should be ascribed to that excessive BiOI amount cause the self-aggregation of nanosheets, thus resulting into the partial overlap on {001} facet of BiOI nanosheets as observed from the above SEM images. I/Cl-2 possessing the largest Zeta potentials (39.8 mV) means that it has the most exposure of {001} facet of BiOI. As the {001} facet is the active facet of BiOI that favors for charge separation, this $\text{BiOI@Bi}_{12}\text{O}_{17}\text{Cl}_2$ front-lateral surfaces coupling assembly architecture is destined to promote the photochemical reactions.

Specific surface areas of samples were determined by the nitrogen adsorption BET method. The specific surface areas of $\text{Bi}_{12}\text{O}_{17}\text{Cl}_2$, I/Cl-1, I/Cl-2, I/Cl-3, I/Cl-4 and BiOI are 6.5, 13.4, 26.1, 22.2, 18.9 and $15.3 \text{ m}^2/\text{g}$, respectively. These values are consistent with the order of their Zeta potentials. It can be seen that the specific surface areas first increase and then decrease with raising the BiOI amount in the composites. Thus, it can be concluded that appropriate content of $\text{Bi}_{12}\text{O}_{17}\text{Cl}_2$ can serve as an excellent substrate to

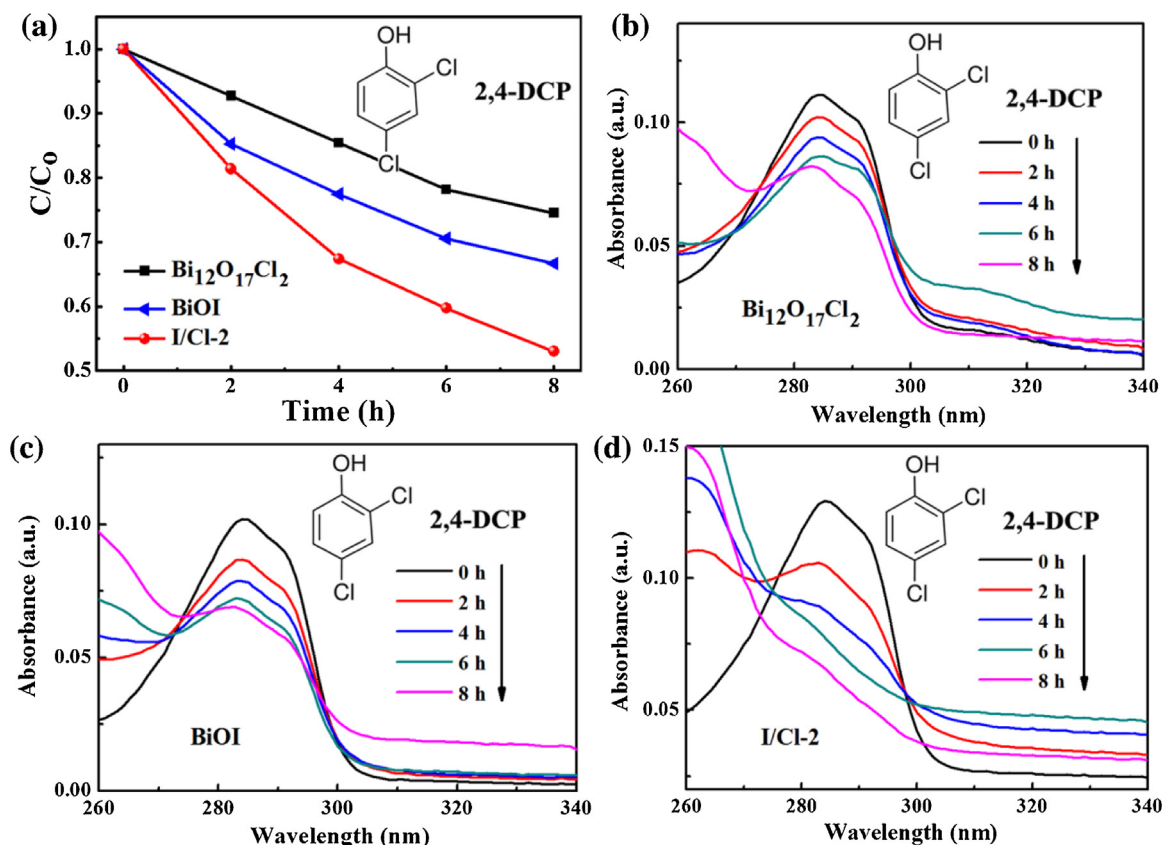


Fig. 10. (a) Photocatalytic degradation curves of 2,4-DCP over BiOI, $\text{Bi}_{12}\text{O}_{17}\text{Cl}_2$ and $\text{BiOI@Bi}_{12}\text{O}_{17}\text{Cl}_2$ composites under visible light ($\lambda > 420 \text{ nm}$); absorption spectra of 2,4-DCP catalyzed by (b) $\text{Bi}_{12}\text{O}_{17}\text{Cl}_2$, (c) BiOI and (d) I/Cl-2.

support and evenly distribute the BiOI nanosheets, which enables increased specific surface areas for enhanced absorption and photocatalytic reactions.

3.3. Optical absorption and energy band structure analyses

The optical absorption of $\text{Bi}_{12}\text{O}_{17}\text{Cl}_2$, BiOI and $\text{BiOI@Bi}_{12}\text{O}_{17}\text{Cl}_2$ architectures is investigated by DRS spectra. As shown in Fig. 6a, the absorption edge of $\text{Bi}_{12}\text{O}_{17}\text{Cl}_2$ is approximately 520 nm, and that of BiOI is located at 670 nm. As for the $\text{BiOI@Bi}_{12}\text{O}_{17}\text{Cl}_2$ composites, their light absorption gradually strengthens with increasing the BiOI content, and the absorption edges ranges from 640 to 660 nm. Thus, the $\text{BiOI@Bi}_{12}\text{O}_{17}\text{Cl}_2$ composites still possess strong photoabsorption ability in visible region, which favors for the generation of photoinduced charges. The optical band gaps of $\text{Bi}_{12}\text{O}_{17}\text{Cl}_2$ and BiOI can be obtained from their DRS spectra. Determined from the plots of $(\alpha h\nu)^{1/2}$ versus $(h\nu)$, the band gaps of BiOI and $\text{Bi}_{12}\text{O}_{17}\text{Cl}_2$ are estimated to be 1.76 eV and 2.22 eV, respectively (Fig. 6b). Though band gap mainly reflects the property of a single semiconductor, we estimate the band energy of I/Cl-2, which is approximately 1.78 eV.

As the photocatalytic activity of semiconductor composite photocatalysts is closely associated with the semiconductor types and their conduction band (CB) and valence band (VB), Mott–Schottky (M–S) measurements are performed to determine the band energy levels as well as semiconductor types [43]. As seen from Fig. 7, the flat band (FB) potential of $\text{Bi}_{12}\text{O}_{17}\text{Cl}_2$ is about -0.58 V versus a saturated calomel electrode (SCE), equal to -0.34 V vs. a normal hydrogen electrode (NHE). Meanwhile, the positive slope of linear $1/C^2$ potential curve demonstrates that $\text{Bi}_{12}\text{O}_{17}\text{Cl}_2$ is a n-type semiconductor. As the FB of n-type semiconductor is situated close to the conduction band (CB) position, the latter can be estimated (0.1–0.3 eV above FB) [44]. Thus, the CB and VB positions

of $\text{Bi}_{12}\text{O}_{17}\text{Cl}_2$ are estimated to be -0.44 and 1.95 eV , respectively. In our previous report, we have measured the M–S curve of the BiOI nanosheets synthesized by EG-assisted precipitation method, which indicated that BiOI is a p-type semiconductor with FB of 2.14 V (NHE) [35]. Accordingly, the CB and VB levels are calculated to be 0.48 and 2.24 eV , respectively.

3.4. Photocatalytic activity enhancement

3.4.1. Photodegradation of RhB

The photocatalytic performance of $\text{Bi}_{12}\text{O}_{17}\text{Cl}_2$, BiOI and $\text{BiOI@Bi}_{12}\text{O}_{17}\text{Cl}_2$ composites is first evaluated by degradation of RhB with irradiation of visible light ($\lambda > 420 \text{ nm}$). The adsorption efficiencies of RhB on $\text{Bi}_{12}\text{O}_{17}\text{Cl}_2$, BiOI and $\text{BiOI@Bi}_{12}\text{O}_{17}\text{Cl}_2$ composites in darkness are consistent with the order of their specific surface areas (Fig. S1). As seen from Fig. 8a, $\text{Bi}_{12}\text{O}_{17}\text{Cl}_2$ shows a weak photocatalytic activity, and only 20% of RhB was degraded within 5 h. Comparatively, BiOI presents a high photocatalytic activity with a degradation efficiency of 91%. With regard to the $\text{BiOI@Bi}_{12}\text{O}_{17}\text{Cl}_2$ composites, all of them showed enhanced degradation performance in comparison with the pure BiOI and $\text{Bi}_{12}\text{O}_{17}\text{Cl}_2$. As revealed by the pseudo-first-order kinetics of the samples (Fig. 8b), the apparent rate constants of $\text{Bi}_{12}\text{O}_{17}\text{Cl}_2$, I/Cl-1, I/Cl-2, I/Cl-3, I/Cl-4 and BiOI are 0.041 h^{-1} , 0.575 h^{-1} , 0.937 h^{-1} , 0.676 h^{-1} , 0.492 h^{-1} and 0.454 h^{-1} , respectively. The photocatalytic activity first increases and then declines, and I/Cl-2 displays the optimum photoreactivity, which is 22.8 and 2.1 times higher than that of pristine $\text{Bi}_{12}\text{O}_{17}\text{Cl}_2$ and BiOI, respectively. The activity difference of samples may be closely related to the microstructure of composites, which would be discussed in the following. The mineralization ratio of RhB over I/Cl-2 was determined by conducting a total organic carbon (TOC) analysis. As shown in Fig. 9, after 5 h

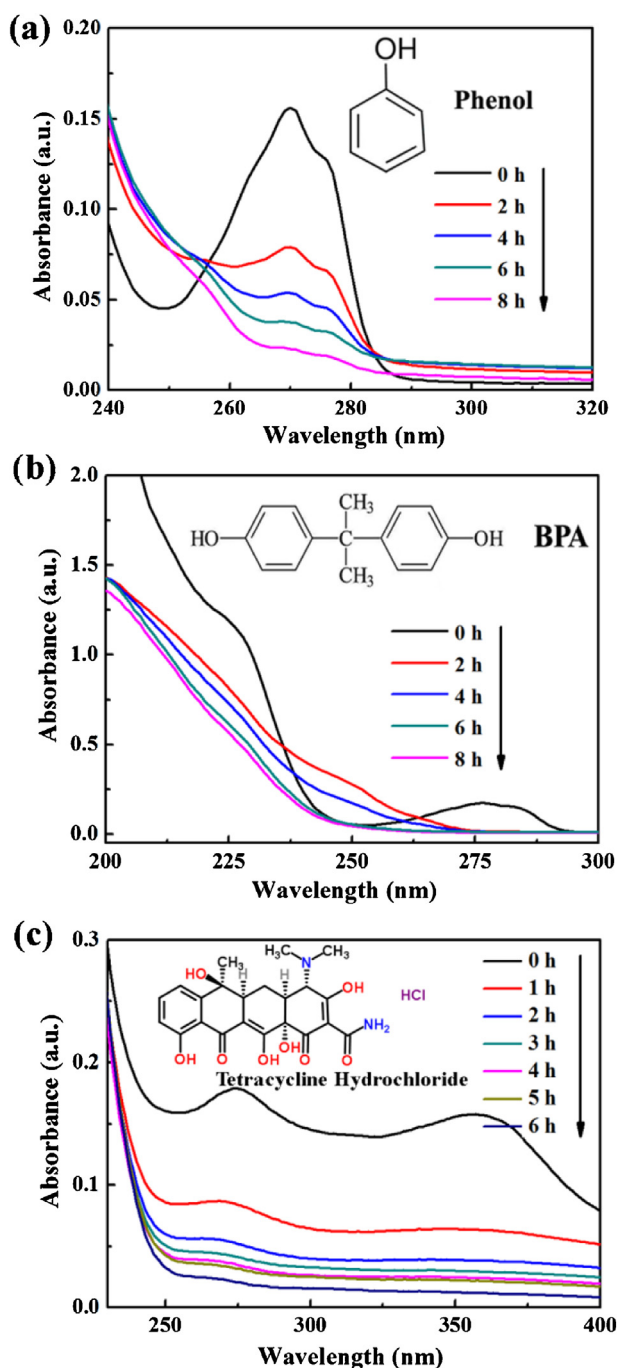


Fig. 11. Time-resolved absorption spectra of (a) phenol, (b) bisphenol A (BPA) and (c) tetracycline hydrochloride degraded by I/Cl-2 under visible light ($\lambda > 420$ nm) illumination.

visible-light irradiation, the removal efficiency of TOC was approximately 63.2%, which indicates that 63.2% of organic carbon from RhB can be mineralized to be CO_2 . It confirmed that the degradation process of RhB by $\text{BiOI@Bi}_{12}\text{O}_{17}\text{Cl}_2$ composites is through photo-oxidation induced decomposition.

3.4.2. Photodegradation of 2,4-dichlorophenol

2,4-Dichlorophenol (2,4-DCP), which is a poisonous pollutant to aquatic life and cannot absorb visible light, was chosen to verify the enhanced photocatalytic property of $\text{BiOI@Bi}_{12}\text{O}_{17}\text{Cl}_2$ composite under visible light ($\lambda > 420$ nm). It can be found that 2,4-DCP is almost not adsorbed by $\text{Bi}_{12}\text{O}_{17}\text{Cl}_2$, BiOI and I/Cl-2 (Fig. S2). Under

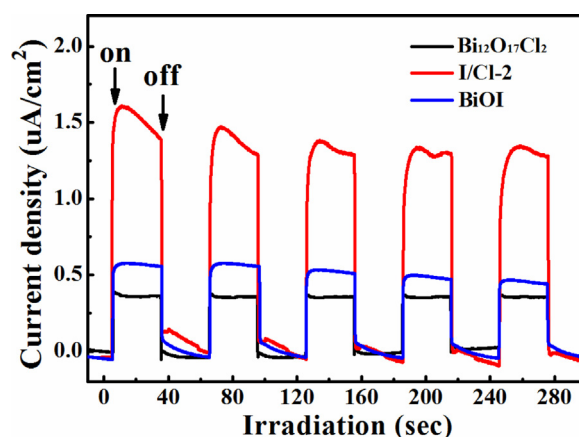


Fig. 12. Transient photocurrent responses for $\text{Bi}_{12}\text{O}_{17}\text{Cl}_2$, BiOI and I/Cl-2 ($[\text{Na}_2\text{SO}_4] = 0.1$ M).

8 h visible-light-irradiation, $\text{Bi}_{12}\text{O}_{17}\text{Cl}_2$ and BiOI can only degrade 25.5% and 33.4% of 2,4-DCP, as shown in Fig. 10a. Notably, I/Cl-2 shows an obviously improved photocatalytic performance with a 2,4-DCP degradation efficiency of 47%. Fig. 10b–d shows the time-resolved absorption spectra of 2,4-DCP catalyzed by $\text{Bi}_{12}\text{O}_{17}\text{Cl}_2$, BiOI and I/Cl-2, respectively. Compared with those of the two pristine samples, it is clear that the absorption peak of 2,4-DCP at 284 nm displays a larger decline in the presence of $\text{BiOI@Bi}_{12}\text{O}_{17}\text{Cl}_2$ architecture. This result demonstrates the improvement on photo-reactivity furnished by the $\text{BiOI@Bi}_{12}\text{O}_{17}\text{Cl}_2$ heterostructure.

3.4.3. Photodegradation of diverse industrial contaminants and antibiotic

In order to further reveal the photooxidation capability of $\text{BiOI@Bi}_{12}\text{O}_{17}\text{Cl}_2$ composite, several industrial contaminants and pharmaceutical, which can cause antibiotic-resistant pathogens development or reproductive abnormalities, such as bisphenol A (BPA), phenol and tetracycline hydrochloride, are employed herein to be the probing reactant. Compared with phenol and BPA, I/Cl-2 has a relatively strong adsorption effect on tetracycline hydrochloride in darkness (Fig. S3). Fig. 11a–c shows the curves of absorption change of phenol, BPA and tetracycline hydrochloride with visible light illumination ($\lambda > 420$ nm), respectively. One can obviously see that the characteristic absorption bands of phenol (270 nm), BPA (226 nm and 277 nm) and tetracycline hydrochloride (270 nm and 350 nm) gradually decreased with extension of irradiation time. These results disclose that the $\text{BiOI@Bi}_{12}\text{O}_{17}\text{Cl}_2$ heterostructures possess powerful photooxidizing ability, which can be utilized to treat various industrial contaminants and pharmaceuticals.

For reference, photolysis tests of the 2,4-DCP, RhB, BPA, phenol and tetracycline hydrochloride with 8 h visible light irradiation are performed. It can be found that they are all stable under visible light as shown in Fig. S4 (only 2% of tetracycline hydrochloride was decomposed). Thus, the impact of self-photolysis on the photocatalytic performance can be ruled out.

Meanwhile, the TOC removal efficiencies of 2,4-DCP, BPA, phenol and tetracycline hydrochloride over I/Cl-2 are also determined. As seen from Fig. S5, their TOC removal efficiencies gradually increase with prolonging the illumination time and are close to the values obtained from the absorption spectra. It indicates that most of the pollutants are mineralized to small inorganic molecules, like CO_2 and H_2O under the photocatalytic degradation process, further revealing the strong photo-oxidation capability of $\text{BiOI@Bi}_{12}\text{O}_{17}\text{Cl}_2$ heterojunction.

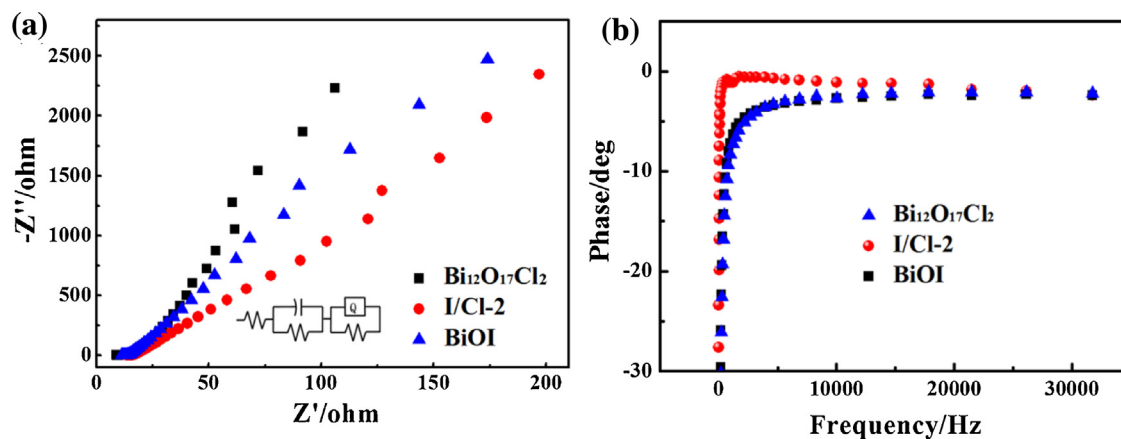


Fig. 13. (a) EIS Nyquist plots (the inset shows the equivalent $R(\text{RC})(\text{RQ})$ circuits) and (b) bode-phase curves of $\text{Bi}_{12}\text{O}_{17}\text{Cl}_2$, BiOI and I/Cl-2 under visible light irradiation ($[\text{Na}_2\text{SO}_4] = 0.1 \text{ M}$).

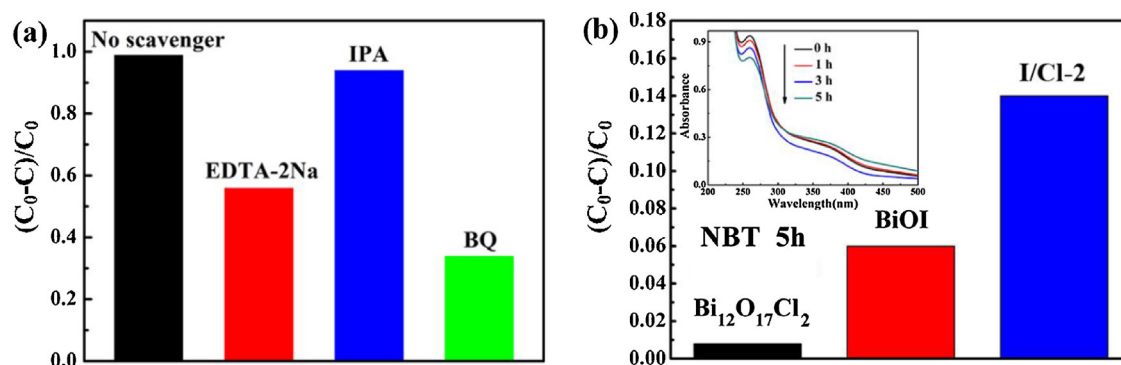


Fig. 14. (a) Photodegradation of RhB on I/Cl-2 with different scavengers; (b) transformation percentage of NBT concentration after 5 h visible light irradiation ($\lambda > 420 \text{ nm}$) by $\text{Bi}_{12}\text{O}_{17}\text{Cl}_2$, BiOI and I/Cl-2 (the inset shows the change of absorption spectra of NBT).

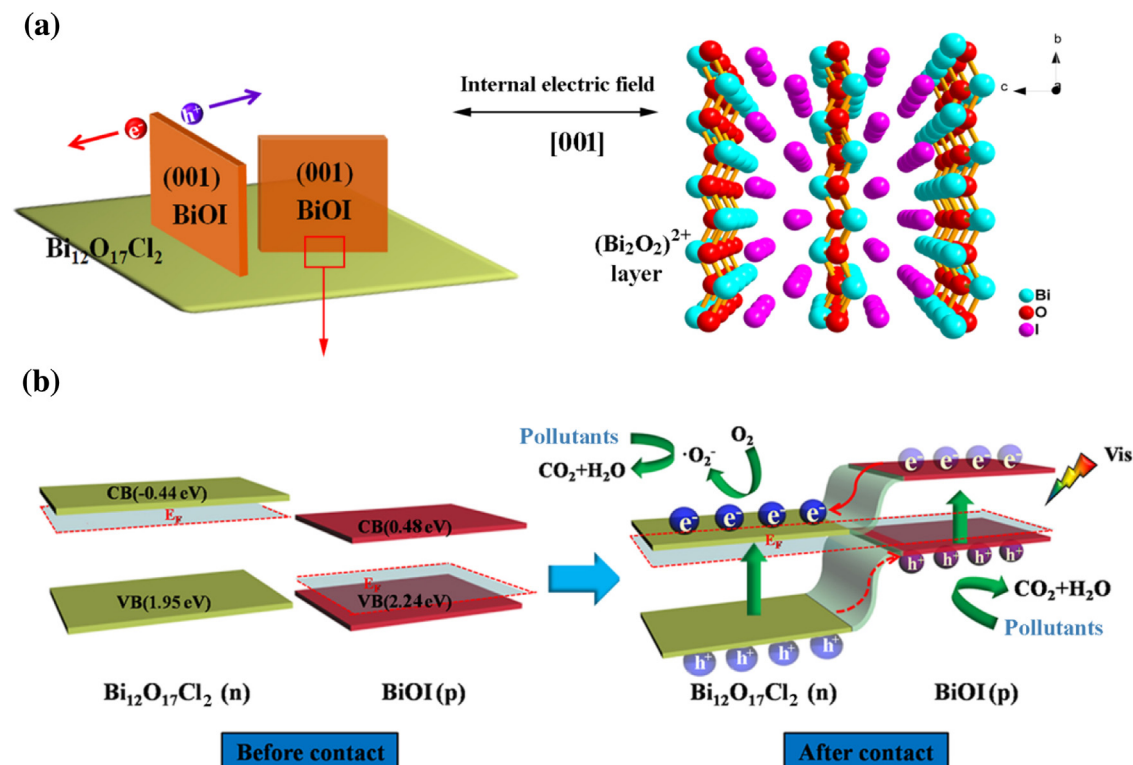


Fig. 15. Schematic diagrams for (a) efficient charge separation process through the {001} active facets of BiOI and (b) the proposed charge transfer mechanism via $\text{BiOI}@\text{Bi}_{12}\text{O}_{17}\text{Cl}_2$ p-n junction.

3.5. Charge separation and photocatalytic enhancement mechanism

To elucidate the high photo-activity of BiOI@Bi₁₂O₁₇Cl₂, photocurrent production is employed herein to survey the separation and movement dynamics of photoinduced charge carriers of Bi₁₂O₁₇Cl₂, BiOI and BiOI@Bi₁₂O₁₇Cl₂ (I/Cl-2) photoelectrodes [45,46]. As shown in Fig. 12, all the three photoelectrodes display stable and reversible photocurrent response. The immediate appearance of current signals with light on indicates the high sensitivity to light. In contrast to Bi₁₂O₁₇Cl₂ and BiOI, I/Cl-2 presents drastically enhanced current density, which is 2.5 and 3.8 times as high as that of them, respectively. The photocurrent measurements illustrates that separation of photogenerated electron-hole pairs is profoundly facilitated at the interface between BiOI and Bi₁₂O₁₇Cl₂.

For further verifying the efficient separation of photogenerated charge carriers, we measured the electrochemical impedance spectra (EIS) of Bi₁₂O₁₇Cl₂, BiOI and I/Cl-2. As shown in Fig. 13a, I/Cl-2 displays an obviously smaller arc radius in the EIS Nyquist plots in comparison with the pure BiOI and Bi₁₂O₁₇Cl₂. It demonstrates that I/Cl-2 has a lower interfacial layer resistance, and thus a higher charge transfer efficiency [45,46]. Besides, we can estimate the lifetime (τ) of the injected electrons from the conduction band of semiconductor photocatalysts by using the equation $\tau \approx 1/(2\pi f)$, where f indicates the inverse minimum frequency [47]. Fig. 13b shows the Bode-phase plots of Bi₁₂O₁₇Cl₂, BiOI and I/Cl-2. Their electron lifetimes are determined to be 117 μ s, 72.7 μ s and 54.9 μ s for I/Cl-2, BiOI and Bi₁₂O₁₇Cl₂, respectively. The largely increased lifetime (τ) of the injected electrons of BiOI@Bi₁₂O₁₇Cl₂ architecture confirms the promoted interfacial charge transfer. The above results evidence that the high separation and fast transfer of photogenerated electron-hole pairs are responsible for the promoted photocatalytic activity of BiOI@Bi₁₂O₁₇Cl₂ heterostructure.

Efficient separation of charge carriers is bound to result in the increment of an active species amount. In order to provide convincing evidence for that the enhanced photocatalytic activity originates from the enhanced active radicals, active species trapping and NBT transformation experiments are conducted. As shown in Fig. 14a and Fig. S6, the RhB degradation is practically not influenced with addition of IPA as a quencher of $\cdot\text{OH}$. By contrast, the addition of BQ (a quencher of $\cdot\text{O}_2^-$) and EDTA-2Na (a quencher of h^+) significantly reduce the degradation rate of RhB. Thus, it can be inferred that, in the photodegradation process of BiOI@Bi₁₂O₁₇Cl₂, $\cdot\text{O}_2^-$ is the most leading active species, and h^+ comes next. To quantitatively understand and compare the active species generated by BiOI@Bi₁₂O₁₇Cl₂ architecture and the two individual components, herein NBT was employed as the molecular probe to quantify $\cdot\text{O}_2^-$ production by reacting with $\cdot\text{O}_2^-$. Fig. 14b displays the transformation percentage of NBT over I/Cl-2, BiOI and Bi₁₂O₁₇Cl₂ with 5 h illumination of visible light ($\lambda > 420\text{ nm}$). Compared the low NBT transformation percentage of Bi₁₂O₁₇Cl₂ (0.8%) and BiOI (5.9%), I/Cl-2 shows a considerably enhanced transformation percentage of NBT, which is as high as 14.1%. For reference, NBT transformation with 5 h direct visible light irradiation ($\lambda > 420\text{ nm}$) in the absence of photocatalysts was performed. As shown in Fig. S7, almost no NBT transformation occurred. It confirmed that the active $\cdot\text{O}_2^-$ is generated from the photocatalysts under photo-excitation. This result established that the efficient separation of electrons and holes derived from the BiOI@Bi₁₂O₁₇Cl₂ heterostructure causes the generation of abundant robust active species, resulting in the greatly improved photooxidizing capability.

According to the above results, the greatly promoted photocatalytic activity of BiOI@Bi₁₂O₁₇Cl₂ should be mainly attributed to the following aspects: For one thing, Bi₁₂O₁₇Cl₂ can serve as an excellent substrate to support and evenly distribute the BiOI nanosheets, which enables increased specific surface areas for

enhanced absorption and more reaction active sites. However, the increased level of specific surface areas is lower than the enhancement level of photocatalytic activity. Thus, other advantages in the BiOI@Bi₁₂O₁₇Cl₂ composite must play important roles. For another, the front-lateral surfaces coupling assembly of BiOI@Bi₁₂O₁₇Cl₂ architecture enables more exposure of {001} facets of BiOI. Due to the intensive photoabsorption capability, substantial photogenerated electron-hole pairs appear under visible light illumination. Driven by the strong self-built electric field derived from the {001} active facets of BiOI, these as-generated electrons and holes rapidly migrate from the inside to the surface of BiOI nanosheets, and then are gathered at the opposite surfaces, like the top surface and bottom surface, respectively, as shown in Fig. 15a. Therefore, the photogenerated electron-hole pairs of BiOI nanosheets are efficiently separated along the [001] direction. Moreover, the efficient charge transfer at the interface between BiOI and Bi₁₂O₁₇Cl₂ also contributes to the high photocatalytic activity of BiOI@Bi₁₂O₁₇Cl₂ composite. As displayed in the above results, the p-type BiOI and n-type Bi₁₂O₁₇Cl₂ can form a steady *p-n* junction. Before contact, the CB and VB of BiOI are lower than those of Bi₁₂O₁₇Cl₂ (Fig. 15b). After construction of *p-n* junction, the energy levels of Bi₁₂O₁₇Cl₂ down-shift, whereas those of BiOI up-shift till the Fermi levels (E_F) equilibrium between BiOI and Bi₁₂O₁₇Cl₂ was achieved. Finally, the CB bottom and VB top of BiOI are higher than those of Bi₁₂O₁₇Cl₂. Driven by the potential difference, the photogenerated electrons from the CB of BiOI can quickly migrate to that of Bi₁₂O₁₇Cl₂, and simultaneously the holes produced from the VB of Bi₁₂O₁₇Cl₂ are transferred onto that of BiOI. Thus, the electrons-hole pairs are efficiently separated over the BiOI@Bi₁₂O₁₇Cl₂ *p-n* junction, and the holes pooled in the VB of Bi₁₂O₁₇Cl₂ directly oxidate the pollutants. The electrons gathered at the CB of BiOI are further transformed into $\cdot\text{O}_2^-$ with powerful oxidation ability, subsequent inducing the decomposition of various contaminants.

4. Conclusion

p-n junction BiOI@Bi₁₂O₁₇Cl₂ heterostructure was fabricated by a facile *in situ* precipitation of BiOI nanosheets onto Bi₁₂O₁₇Cl₂. In this heterostructure, BiOI nanosheets are assembled on Bi₁₂O₁₇Cl₂ in a front-lateral surfaces coupling way due to the charge induction, thus resulting in large exposure of {001} reactive exposing facets of BiOI. The as-obtained BiOI@Bi₁₂O₁₇Cl₂ heterostructure shows much enhanced visible-light photocatalytic performance toward degradation of RhB and 2,4-DCP in contrast to the pure samples. In particular, it also presents powerful photo-oxidation ability in treating multiple industrial pollutants and antibiotic bisphenol A, phenol and tetracycline hydrochloride. Photoelectrochemical measurements revealed that the dramatically strengthened photocatalytic activity is attributed to the high separation and transfer efficiency derived from the BiOI {001} active facets and *p-n* junction of BiOI@Bi₁₂O₁₇Cl₂ heterostructure. Radicals detection and quantification experiments confirmed the elevated $\cdot\text{O}_2^-$ amount generated from BiOI@Bi₁₂O₁₇Cl₂ heterostructure. The current work illustrate a facile protocol to combine the active exposing facets with semiconductor *p-n* junction to develop new heterostructured photocatalysts.

Competing interest

The authors declare no competing financial interest.

Acknowledgements

This work was jointly supported by the National Natural Science Foundations of China (Grant Nos. 51302251 and 51572246),

the Fundamental Research Funds for the Central Universities (2652013052 and 2652015296).

Appendix A. Supplementary data

Supplementary data associated with this article can be found, in the online version, at <http://dx.doi.org/10.1016/j.apcatb.2016.06.020>.

References

- [1] A. Kubacka, M. Fernández-García, G. Coloin, *Chem. Rev.* 112 (2012) 1555–1614.
- [2] Y.F. Zhao, G.B. Chen, T. Bian, C. Zhou, G.I.N. Waterhouse, L.Z. Wu, C.H. Tung, L.J. Smith, D. O'Hare, T.R. Zhang, *Adv. Mater.* 27 (2015) 7823.
- [3] L. Shang, T. Bian, B. Zhang, D.H. Zhang, L.Z. Wu, C.H. Tung, Y.D. Yin, T.R. Zhang, *Angew. Chem. Int. Ed.* 53 (2014) 250–254.
- [4] H. Tong, S.X. Ouyang, Y.P. Bi, N. Umezawa, M. Oshikiri, J.H. Ye, *Adv. Mater.* 24 (2012) 229–251.
- [5] S.Y. Dong, J.L. Feng, Y.K. Li, L.M. Hu, M.L. Liu, Y.F. Wang, Y.Q. Pi, J.Y. Sun, J.H. Sun, *Appl. Catal. B: Environ.* 152–153 (2014) 413–424.
- [6] S.Y. Dong, J.L. Feng, M.H. Fan, Y.Q. Pi, L.M. Hu, X. Han, M.L. Liu, J.Y. Sun, J.H. Sun, *RSC Adv.* 5 (2015) 14610–14630.
- [7] X. Li, J.G. Yu, M. Jaroniec, *Chem. Soc. Rev.* (2016), <http://dx.doi.org/10.1039/C5CS00838G>.
- [8] H.L. Wang, L.S. Zhang, Z.G. Chen, J.Q. Hu, S.J. Li, Z.H. Wang, J.S. Liu, X.C. Wang, *Chem. Soc. Rev.* 43 (2014) 5234–5244.
- [9] X. Wang, Q. Xu, M.R. Li, S. Shen, X.L. Wang, Y.C. Wang, Z.C. Feng, J.Y. Shi, H.X. Han, C. Li, *Angew. Chem. Int. Ed.* 51 (2012) 13089–13092.
- [10] Y.X. Guo, H.W. Huang, Y. He, N. Tian, T.R. Zhang, P.K. Chu, Q. An, Y.H. Zhang, *Nanoscale* 7 (2015) 11702–11711.
- [11] N. Tian, H.W. Huang, C.Y. Liu, F. Dong, T.R. Zhang, X. Du, S.X. Yu, Y.H. Zhang, *J. Mater. Chem. A* 3 (2015) 17120–17129.
- [12] X.X. Chang, T. Wang, P. Zhang, J.J. Zhang, A. Li, J.L. Gong, *J. Am. Chem. Soc.* 137 (2015) 8356–8359.
- [13] X. Yu, J. Zhang, Z. Zhao, W.B. Guo, J.C. Qiu, X.N. Mou, A.X. Li, J.P. Claveried, H. Liu, *Nano Energy* 16 (2015) 207–217.
- [14] M. D'Arienzo, J. Carbajo, A. Bahamonde, M. Crippa, S. Polizzi, R. Scotti, L. Wahba, F. Morazzoni, *J. Am. Chem. Soc.* 133 (2011) 17652–17661.
- [15] T.R. Gordon, M. Cargnello, T. Paik, F. Mangolini, R.T. Weber, P. Fornasiero, C.B. Murray, *J. Am. Chem. Soc.* 134 (2012) 6751–6761.
- [16] J.G. Yu, J.X. Low, W. Xiao, P. Zhou, M. Jaroniec, *J. Am. Chem. Soc.* 136 (2014) 8839–8842.
- [17] H.F. Cheng, B.B. Huang, Y. Dai, *Nanoscale* 6 (2014) 2009–2026.
- [18] J. Li, Y. Yu, L.Z. Zhang, *Nanoscale* 6 (2014) 8473–8488.
- [19] H. Li, J. Shang, Z.H. Ai, L.Z. Zhang, *J. Am. Chem. Soc.* 137 (2015) 6393–6399.
- [20] L.M. Hu, S.Y. Dong, Q.L. Li, J.L. Feng, Y.Q. Pi, M.L. Liu, J.Y. Sun, J.H. Sun, *J. Alloys Compd.* 633 (2015) 256–264.
- [21] S.Y. Dong, Y.Q. Pi, Q.L. Li, L.M. Hu, Y.K. Li, X. Han, J.Z. Wang, J.H. Sun, *J. Alloys Compd.* 663 (2016) 1–9.
- [22] J. Li, L.Z. Zhang, Y.J. Li, Y. Yu, *Nanoscale* 6 (2014) 167–171.
- [23] X.Y. Xiao, J. Jiang, L.Z. Zhang, *Appl. Catal. B: Environ.* 142 (2013) 487–493.
- [24] J.L. Wang, Y. Yu, L.Z. Zhang, *Appl. Catal. B: Environ.* 136 (2013) 112–121.
- [25] S.M. Sun, W.Z. Wang, L. Zhang, L. Zhou, W.Z. Yin, M. Shang, *Environ. Sci. Technol.* 43 (2009) 2005–2010.
- [26] X. Xiao, C.L. Xing, G.P. He, X.X. Zuo, J.M. Nan, L.S. Wang, *Appl. Catal. B: Environ.* 148 (2014) 154–163.
- [27] L.Q. Ye, J.N. Chen, L.H. Tian, J.Y. Liu, T.Y. Peng, K.J. Deng, L. Zan, *Appl. Catal. B: Environ.* 130–131 (2013) 1–7.
- [28] J.X. Xia, S. Yin, H.M. Li, H. Xu, Y.S. Yan, Q. Zhang, *Langmuir* 27 (2011) 1200–1206.
- [29] X. Zhang, L.Z. Zhang, T.F. Xie, D.J. Wang, *J. Phys. Chem. C* 133 (2009) 7371–7378.
- [30] J. Jiang, X. Zhang, P.B. Sun, L.Z. Zhang, *J. Phys. Chem. C* 115 (2011) 20555–20564.
- [31] J. Cao, B.Y. Xu, H.L. Lin, S.F. Chen, *Chem. Eng. J.* 228 (2013) 482–488.
- [32] X. Xiao, R. Hao, M. Liang, X.X. Zuo, J.M. Nan, L.S. Li, W.D. Zhang, *J. Hazard. Mater.* 233–234 (2012) 122–130.
- [33] J. Cao, B.Y. Xu, H.L. Lin, B.D. Luo, S.F. Chen, *Chem. Eng. J.* 185–186 (2012) 91–99.
- [34] K.H. Ye, Z.S. Chai, J.W. Gu, X. Yu, C.X. Zhao, Y.M. Zhang, W.J. Mai, *Nano Energy* 18 (2015) 222–231.
- [35] H.W. Huang, Y. He, X. Du, P.K. Chu, Y.H. Zhang, *ACS Sustain. Chem. Eng.* 3 (2015) 3262–3273.
- [36] L.M. Sun, L. Xiang, X. Zhao, C.J. Jia, J. Yang, Z. Jin, X.F. Cheng, W.L. Fan, *ACS Catal.* 5 (2015) 3540–3551.
- [37] F. Dong, T. Xiong, Y.J. Sun, Y.X. Zhang, Y. Zhou, *Chem. Comm.* 51 (2015) 8249–8252.
- [38] H.W. Huang, X. Han, X.W. Li, S.C. Wang, P.K. Chu, Y.H. Zhang, *ACS Appl. Mater. Interfaces* 7 (2015) 482–492.
- [39] H.W. Huang, X.W. Li, X. Han, N. Tian, Y.H. Zhang, T.R. Zhang, *Phys. Chem. Chem. Phys.* 17 (2015) 3673–3679.
- [40] H.W. Huang, K. Liu, Y.L. Zhang, K. Chen, Y.H. Zhang, N. Tian, *RSC Adv.* 4 (2014) 49386–49394.
- [41] L.Q. Ye, J.Y. Liu, C.Q. Gong, L.H. Tian, T.Y. Peng, L. Zan, *ACS Catal.* 2 (2012) 1677–1683.
- [42] L.Q. Ye, J.Y. Liu, Z. Jiang, T.Y. Peng, L. Zan, *Appl. Catal. B: Environ.* 142–143 (2013) 1–7.
- [43] H.W. Huang, X.W. Li, J.J. Wang, F. Dong, P.K. Chu, T.R. Zhang, Y.H. Zhang, *ACS Catal.* 5 (2015) 4094–4103.
- [44] H.W. Huang, K. Xiao, S.X. Yu, F. Dong, T.R. Zhang, Y.H. Zhang, *Chem. Comm.* 52 (2015) 354–357.
- [45] X.J. Bai, L. Wang, Y.F. Zhu, *ACS Catal.* 2 (2012) 2769–2778.
- [46] H.W. Huang, Y. He, Z.S. Lin, L. Kang, Y.H. Zhang, *J. Phys. Chem. C* 117 (2013) 22986–22994.
- [47] S.M. Sun, W.Z. Wang, L. Zhang, *J. Phys. Chem. C* 117 (2013) 9113–9120.